

Chapter 1

High-Resolution Optical and Confocal Microscopy

Olaf Hollricher and Wolfram Ibach

Abstract In this chapter, the theory of optical image formation in an optical microscope is described, and the difference between conventional and confocal microscopy is explained. The selection of the appropriate pinhole diameter is discussed in detail, as the pinhole diameter is crucial in obtaining the highest depth resolution as well as optimizing collection efficiency, because the Raman signal is typically very weak.

1.1 Introduction

More than 2000 years ago, Seneca¹ described the magnifying properties of water-filled glass spheres. Since that time, many researchers have known that all convex lenses can be used to magnify objects, but it took more than a millennium until further improvements led to the combination of several lenses to form an optical microscope. It is often said that Dutch spectacle maker Hans Janssen and his son Zacharias² were the first to develop the optical microscope by combining several lenses to form an optical microscope. It could, however, also have been the Dutch-German lens maker Hans Lippershey³ or even Galileo Galilei.⁴ Galileo combined a convex and a concave lens for his microscopes in 1609. Christiaan Huygens,⁵ also a Dutch scientist, developed the first achromatic objective in the late 17th century by combining two lenses of different kinds of glass, which was a big step forward.

Up to the 19th century, progress in quality and resolution was slow because microscopes were built using experience and trial and error, not using scientific knowledge.

¹ Lucius Annaeus Seneca the younger (* around 4 BC, † 65 AD).

² Zacharias Janssen (* around 1588, † around 1631).

³ Hans Lippershey (* around 1570, † September 1619).

⁴ Galileo Galilei (* 15.02.1564, † 08.01.1642).

⁵ Christiaan Huygens (* 14.04.1629, † 08.07.1695).

Around 1873, Ernst Abbe,⁶ Prof. of Physics in Jena, Germany, developed his theory of optical image formation which was the basis of understanding the physics behind the optical microscope. His combined work with Carl Zeiss,⁷ who was a precision mechanic and Otto Schott,⁸ who had a PhD in chemistry and used his knowledge to develop glass with different optical properties, led to the development of the diffraction-limited optical microscope as it is known today. The resolution of the optical microscope remained nearly constant since the advent of Abbe's diffraction theory and is still about half of the wavelength of the excitation light.

During the 20th century, many new imaging techniques were introduced, such as fluorescence microscopy, interference microscopy, phase contrast, and dark-field illumination which made the optical microscope a powerful analytical tool, but the most important development of recent years is the confocal microscope.⁹

The principle underlying confocal imaging was patented by Marvin Minsky in 1957 (US patent 3013467), but it was not until the late 1980s that it became a standard technique. In confocal microscopy, a point-like light source (typically a laser) is focused onto the sample and the image of this spot is detected through a small pinhole in front of the detector. As the pinhole is located in the image plane of the microscope, the pinhole is confocal with the illuminating spot.

An image of the sample can only be obtained by either scanning the sample or the excitation spot point by point and line by line. This makes a confocal microscope much more complex than a conventional microscope, but the additional complexity is far outweighed by the advantage of having the detected light restricted to a small area around the focal point. Therefore, scattered light from above or below the focal point does not contribute to the image.

Although an increase in lateral resolution of a factor of $\approx 1.4 (\sqrt{2})$ can be achieved by convolution of the excitation spot with the pinhole aperture, this resolution enhancement can only be achieved at a high price: the pinhole must be so small that 95% of the light is lost. The main advantage of confocal microscopy as compared to conventional microscopy is therefore the depth resolution and the much higher image contrast due to stray light suppression.

This chapter provides an introduction to the theory of confocal image formation.

The first section describes the theory of image formation in an optical microscope and the differences between conventional and confocal microscopy are explained. The next section describes the choice of the appropriate pinhole diameter, suitable for highest depth and lateral resolution. Factors that need to be taken into account in order to achieve optimum results will also be explained.

⁶ Ernst Karl Abbe (* 23.1.1840, † 14.1.1905).

⁷ Carl Zeiss (* 11.9.1816, † 3.12.1888).

⁸ Otto Schott (* 17.12.1851, † 27.8.1935).

⁹ "Confocal" from "konfokal": (lat.) with equal focal points.

1.2 Introduction to Theoretical Considerations in High-Resolution Microscopy

All confocal imaging techniques, for example, confocal Raman microscopy or confocal two-photon microscopy are based on a point-to-point image formation. A detailed overview of these methods can be found in [1].

In this section, a theoretical background for this technique will be provided. The electromagnetic field distribution in the focus of an objective will be calculated, which is the starting point for the mathematical description of image formation. Furthermore, the fundamental difference between confocal microscopy and confocal Raman microscopy with its range of excitation possibilities will be discussed.

1.3 Introduction to Confocal Microscopy

In confocal microscopy, a point-like light source is focused with a lens or an objective onto a sample. The spatial extension of the focus spot on the sample is determined by the wavelength λ and the quality of the image formation. The image spot is then focused through the same (or a second) lens onto an aperture (pinhole) in front of a detector. The size of the pinhole is chosen so that only the central part of the focus can pass through the pinhole and reach the detector.

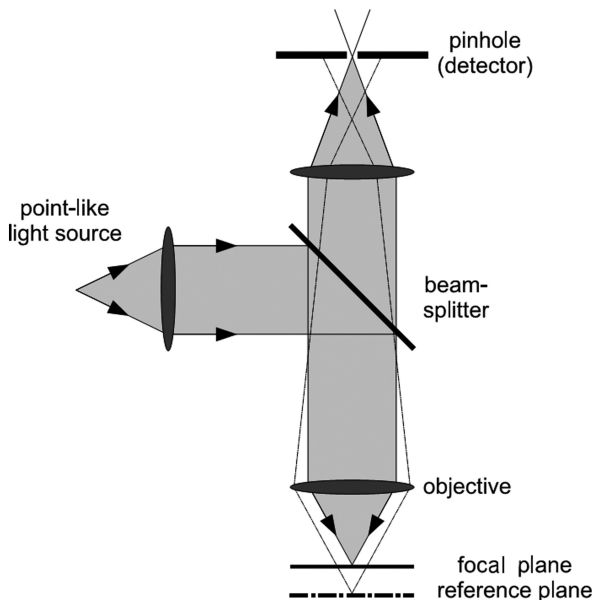


Fig. 1.1 Principal setup of a confocal microscope

One can see in Fig. 1.1 that rays that do not come from the focal plane will not be able to pass through the pinhole. From this simple geometric representation, two advantages of confocal microscopy can already be seen. First, through scanning of the sample with respect to the objective, a 3D image of the sample can be obtained. This is not possible in conventional microscopy. Second, only light from the focal plane will hit the detector. Therefore, image contrast is strongly enhanced.

Additionally, by choosing an appropriate pinhole diameter, the lateral resolution can be increased by up to a factor of $\sqrt{2}$.

1.4 Electromagnetic Scattering in Optical Systems

In this section, the basic principles necessary for calculating the field distribution in the focus are provided. A detailed discussion can be found in the articles of Wolf [2, 3]. Figure 1.2 shows the geometry used to illustrate this.

S_0 is the origin of a monochromatic wave with frequency ω and S_1 its image obtained with geometric ray optics. The field distribution in the focus is described in the Cartesian coordinate system with origin in S_1 . Starting point is the Helmholtz equation

$$\Delta E + k^2 E = 0$$

which describes the space-dependent component of the electrical field:

$$E(P, t) = \Re \left\{ e(P) e^{-i\omega t} \right\}$$

In general, the Helmholtz equation can be satisfied by

$$e(P) = \int_{-\infty}^{\infty} \int_{-\infty}^{\infty} e^{ik(s_x x + s_y y)} \left\{ U(s_x, s_y) e^{iks_z z} + V(s_x, s_y) e^{-iks_z z} \right\} ds_x ds_y \quad (1.1)$$

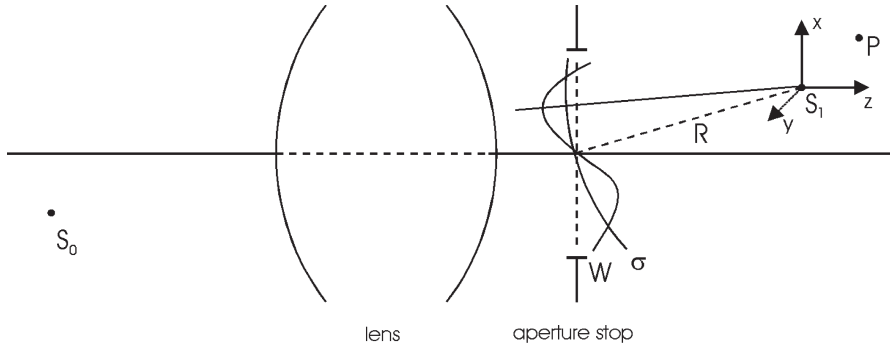


Fig. 1.2 Imaging geometry

where s_z is given by the condition $s_x^2 + s_y^2 + s_z^2 = 1$.

$U(s_x, s_y)$ and $V(s_x, s_y)$ are arbitrary functions that have to fulfill the Kirchhoff boundary conditions. For the magnetic field

$$\mathbf{H}(P, t) = \Re \left\{ \mathbf{h}(P) e^{-i\omega t} \right\}$$

similar expressions can be found.

As described in [2], an approximate solution for the electrical field in the plane of the aperture can be found with the method of stationary phase. This leads to two general solutions:

$$\mathbf{e}(P) = -\frac{ik}{2\pi} \iint_{\Omega} \frac{\mathbf{a}(s_x, s_y)}{s_z} e^{ik\{\Phi(s_x, s_y) + s_x x + s_y y + s_z z\}} ds_x ds_y \quad (1.2)$$

$$\mathbf{h}(P) = -\frac{ik}{2\pi} \iint_{\Omega} \frac{\mathbf{b}(s_x, s_y)}{s_z} e^{ik\{\Phi(s_x, s_y) + s_x x + s_y y + s_z z\}} ds_x ds_y \quad (1.3)$$

Here, the functions $\mathbf{a}(s_x, s_y)$, $\mathbf{b}(s_x, s_y)$, and $\Phi(s_x, s_y)$ take the part of $U(s_x, s_y)$ and $V(s_x, s_y)$. These two functions have the following meaning.

The aberration function $\Phi(s_x, s_y)$ is a measure of how strongly the real wave front W deviates from the ideal spherical wave front σ . The factor $\mathbf{a}(s_x, s_y)$ determines the amplitude of the field. In the geometrical optic, this is the intensity of the light beam. Along every beam $\mathbf{a}(s_x, s_y)$ is independent of the position of the aperture.

All three numbers \mathbf{a} , \mathbf{b} , and Φ can be determined by ray-tracing algorithms.

Equations (1.2) and (1.3) represent the addition of planar waves inside the aperture. In contrast, using the Huygens – Fresnel principle one would add spherical waves.

1.5 3D-Intensity Distribution in the Focus

In the literature one can find two different descriptions for the field distribution in the focus. One describes the electrical field as a scalar and is correct only for small aperture angles. The vector description from Richards and Wolf [4] is more appropriate for the nature of light. Here, the field distribution is a function of the aperture angle α and therefore can also be applied to systems with large aperture angles.

If one compares small and large aperture angles one sees that the electrical energy density in the focal plane is no longer radially symmetric, but depends on the original polarization direction. Additionally, the energy density in the secondary maxima and minima gets larger.

1.5.1 Large Aperture Angles

For an aberration-free system ($\Phi(s_x, s_y) = 0$), a system without wave front errors, all components of the electrical field in the focus can be derived from (1.2) and (1.3). To simplify the calculation the point S_0 (Fig. 1.2) is shifted to infinity. This point is the origin of an electrical field which is polarized in x -direction ($\phi_P = 0$). Therefore, the image of S_0 lies exactly in the focal plane of the lens S_1 . A change of the transmission of the lens due to its surface curvature, which could be calculated with the Fresnel formulas is neglected. Therefore, the surface curvature of the lens must be sufficiently small.

Because of the symmetry of the system, it is appropriate to change to spherical coordinates:

$$x = r_P \sin \theta_P \cos \phi_P, \quad y = r_P \sin \theta_P \sin \phi_P, \quad z = r_P \cos \theta_P$$

The origin of the coordinate system is the geometrical focus point S_1 . We also change to so-called optical coordinates

$$\left. \begin{aligned} u &= k r_P \cos \theta_P \sin^2 \alpha = k z \sin^2 \alpha \\ v &= k r_P \sin \theta_P \sin \alpha = k \sqrt{x^2 + y^2} \sin \alpha \end{aligned} \right\} \quad (1.4)$$

with

$$\begin{aligned} k &= \frac{2\pi}{\lambda} && : \text{absolute value of the wave vector} \\ 0^\circ < \alpha < 90^\circ && : \text{half of the aperture angle} \end{aligned}$$

to eliminate the wavelength dependence. With these coordinates, the spatially dependent components of the electrical and magnetic fields can be written as

$$\left. \begin{aligned} e_x(u, v) &= -iA(I_0 + I_2 \cos 2\phi_P) \\ e_y(u, v) &= -iAI_2 \sin 2\phi_P \\ e_z(u, v) &= -2AI_1 \cos \phi_P \end{aligned} \right\} \quad (1.5)$$

$$\left. \begin{aligned} h_x(u, v) &= -iAI_2 \sin 2\phi_P \\ h_y(u, v) &= -iA(I_0 - I_2 \cos 2\phi_P) \\ h_z(u, v) &= -2AI_1 \sin \phi_P \end{aligned} \right\} \quad (1.6)$$

Herein, I_0 , I_1 , and I_2 are defined over the integrals

$$\left. \begin{aligned} I_0(u, v) &= \int_0^\alpha \cos^{\frac{1}{2}} \theta \sin \theta (1 + \cos \theta) J_0 \left(\frac{v \sin \theta}{\sin \alpha} \right) e^{iu \cos \theta / \sin^2 \alpha} d\theta \\ I_1(u, v) &= \int_0^\alpha \cos^{\frac{1}{2}} \theta \sin^2 \theta J_1 \left(\frac{v \sin \theta}{\sin \alpha} \right) e^{iu \cos \theta / \sin^2 \alpha} d\theta \\ I_2(u, v) &= \int_0^\alpha \cos^{\frac{1}{2}} \theta \sin \theta (1 - \cos \theta) J_2 \left(\frac{v \sin \theta}{\sin \alpha} \right) e^{iu \cos \theta / \sin^2 \alpha} d\theta \end{aligned} \right\} \quad (1.7)$$

The parameter $A = \frac{kfl_0}{2} = \frac{\pi fl_0}{\lambda}$ is a constant containing the focal length f of the lens and the amplitude l_0 of the incoming light. The symbol J_n stands for the Bessel function of order n .

With these equations it is possible to calculate all properties that are important for microscopy. The electrical, magnetic, and total energy distribution have the forms

$$\left. \begin{aligned} \langle w_e(u, v, \phi_P) \rangle &= \frac{A^2}{16\pi} \{ |I_0|^2 + 4|I_1|^2 \cos^2 \phi_P + |I_2|^2 + 2 \cos 2\phi_P \Re(I_0 I_2^*) \} \\ \langle w_m(u, v, \phi_P) \rangle &= \frac{A^2}{16\pi} \{ |I_0|^2 + 4|I_1|^2 \sin^2 \phi_P + |I_2|^2 - 2 \cos 2\phi_P \Re(I_0 I_2^*) \} \\ \langle w(u, v, \phi_P) \rangle &= \frac{A^2}{8\pi} \{ |I_0|^2 + 2|I_1|^2 + |I_2|^2 \} \end{aligned} \right\} \quad (1.8)$$

As expected, the total energy density is independent of the angle ϕ_P . Not as obvious from the equations, but given by the symmetry of the arrangement is that the electrical energy distribution becomes the magnetic energy distribution when turned by 90° .

Also interesting is the Poynting¹⁰ vector \mathbf{S} that describes the energy flux density of the electromagnetic field in the propagation direction. Its time average can be calculated with the equations

$$\left. \begin{aligned} \langle S_x \rangle &= \frac{cA^2}{4\pi} \cos \phi_P \Im \{ I_1 (I_2^* - I_0^*) \} \\ \langle S_y \rangle &= \frac{cA^2}{4\pi} \sin \phi_P \Im \{ I_1 (I_2^* - I_0^*) \} \\ \langle S_z \rangle &= \frac{cA^2}{8\pi} \{ |I_0|^2 - |I_2|^2 \} \end{aligned} \right\} \quad (1.9)$$

For the case of the electrical energy density (1.8) we will discuss what happens to the field distribution with increasing aperture angle. In Fig. 1.3 the electrical energy density is shown in the focal plane ($u = 0$) for different aperture angles α as a function of the optical coordinate v . The case $\alpha = 0^\circ$ corresponds to the case of Sect. 1.5.2, the transition to small aperture angles. For $\alpha = 90^\circ$ the light comes from the complete half space. A cut through the center of the profile, as well as a 10-fold magnification is shown above and to the right of each graphic. The initial polarization of the electrical field is horizontal.

In Fig. 1.3 one can see that the electrical energy density drastically changes with increasing aperture angle. The width of the field distribution as a measure of the optical resolution becomes strongly anisotropic. In the cut through the center, parallel to the direction of polarization, one can see even for small aperture angles that the minima do not return to zero. The side maxima get larger with increasing aperture angle and reach a relative height of 4.3 % for $\alpha = 90^\circ$. This is more than twice the value at $\alpha = 0^\circ$ (1.8 %).

¹⁰ The Poynting vector was defined by John Henry Poynting.

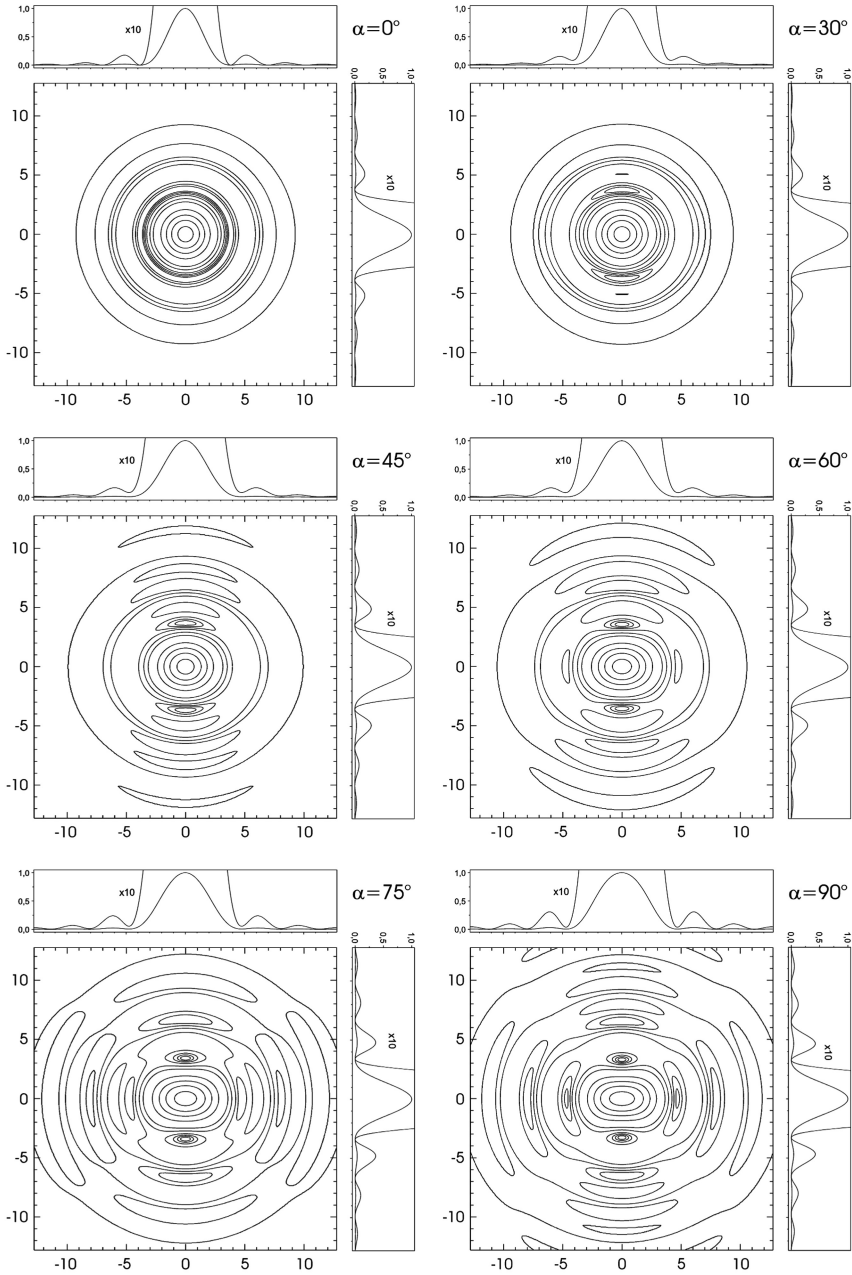


Fig. 1.3 Electrical energy density $w_e(u, v, \phi_p)$ in the focal plane ($u = 0$) for different aperture angles α as a function of v . The initial polarization of the electrical field is horizontal ($\phi_p = 0$). The contour lines show the heights 0.002, 0.005, 0.01, 0.02, 0.05, 0.1, 0.3, 0.5, 0.7, and 0.9. A cut through the center of the profile and a 10-fold magnification are shown above and to the right of each graphic

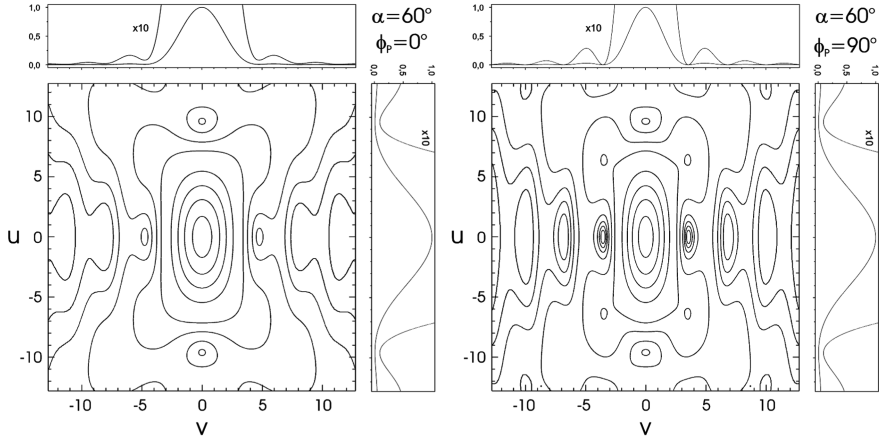


Fig. 1.4 A cut through the electrical energy density $w_e(u, v, \phi_p)$ for $\alpha = 60^\circ$. The optical coordinate u is plotted vertical, while the optical coordinate v is plotted horizontal. In the *left* image, the polarization of the electrical field is horizontal (in the image plane), while in the *right* image it is pointing out of the image plane. The contour lines show the heights 0.002, 0.005, 0.01, 0.02, 0.05, 0.1, 0.3, 0.5, 0.7, and 0.9

Figure 1.4 shows the field distribution in the axial direction. The figure shows a cut through the electrical field distribution w_e vertical to the focal plane. The position of the focusing lens would be above (or below) the figure. In the left image, the polarization of the electrical field is horizontal (in the image plane), while in the right image it is pointing out of the image plane.

Again one can see that the electrical energy distribution is highly anisotropic. Even in the axial direction the minima do not return to zero.

1.5.2 Transition to Small Aperture Angles

The theory in the last paragraph is appropriate to describe vector properties of light, but it is too complicated for a simple understanding. If one permits only small aperture angles I_1 and I_2 can be set zero, because for small x the relation $J_n(x) \sim x^n$ is fulfilled. Equations (1.5) and (1.6) simplify to

$$\begin{aligned} e_x &= h_y = -iA I_0 \\ e_y &= e_z = h_x = h_z = 0 \end{aligned}$$

The initial polarization is preserved for small aperture angles. I_0 can be written so that the integral becomes independent of α

$$\left. \begin{aligned} I_0(u, v) &= \alpha^2 e^{\frac{i u}{\alpha^2}} h(u, v) \\ h(u, v) &= 2 \int_0^1 \rho J_0(\rho v) e^{\frac{1}{2} i u \rho^2} d\rho \end{aligned} \right\} \quad (1.10)$$

The function $h(u, v)$ is called the 3D point spread function (PSF). It is normalized, so that $h(0, 0) = 1$. The PSF can be interpreted as a Greens function that describes the image of an infinitely small point. The approximation of small aperture angles simplifies the theoretical calculation, but is unfortunately coupled with a strong restriction. As a comparison, Fig. 1.5 shows the full width at half maximum (FWHM) of the electrical energy density at $u = 0$ as a function of the aperture angle. The dashed line corresponds to the theory for small aperture angles, whereas the solid lines represent the correct theory for a cut parallel and vertical to the polarization direction. The width of the total energy density w (1.8) is shown as a dotted line. The total energy density w is better suitable for a comparison, because w is radially symmetric, as is the field distribution for small aperture angles.

As expected, all curves are equal for small aperture angles. With increasing α the difference between the curves becomes greater and greater. At an aperture angle of only $\alpha = 40^\circ$ the deviation between the curves is larger than 4%.

Oil- and water-immersion objectives cannot be adequately described by this theory, because their aperture angle is typically between 55° and 70° . For this case, the deviation of the FWHM is more than 10%.

In Fig. 1.5 one can also see that an increase in the aperture angle above 70° results in only a very small increase in resolution. A technical realization above this angle is therefore of little use.

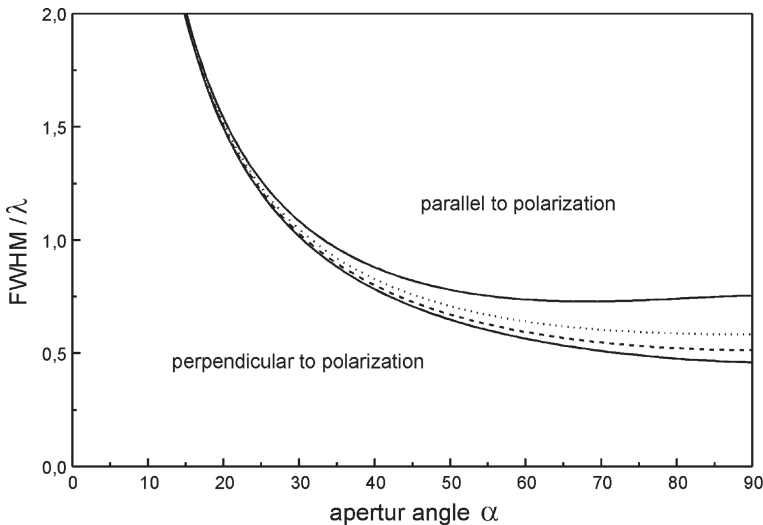


Fig. 1.5 Full width at half maximum (FWHM) of the field distribution in the focal plane; *solid lines*, electrical energy density; *dotted lines*, total energy density; and *dashed lines*, electrical or total energy density for small aperture angles

1.6 Theory of Image Formation

One of the most important properties of a confocal system is the point spread function (PSF), which is mainly determined by the microscope objective. This can be the electrical, magnetic, or total energy density in the focus. If a sample system couples only to the x -component of the electric field, the PSF of the excitation would only contain this component. The PSF of the detection can be different. This depends on the emitted light itself and on the properties of the detector. Of course it would be better if one could measure the PSF for every application. In this case, a deconvolution of the image would be possible without additional assumptions. In [5] a simple interferometric measurement setup is described that makes the measurement of the PSF possible. As a result, one not only finds the amplitude of the function $h(u, v)$ but also the phase. The phase is especially important for a coherent image formation.

In the following paragraphs, h_1 stands for the PSF of the excitation and h_2 for the PSF of the detection. For simplification, both functions should be only scalar values. The modification of the light due to the sample can also be described by the scalar function $\tau(x, y, z)$. In general, τ is a complex function that influences the amplitude and phase of the electromagnetic field.

1.6.1 Microscope

The formation of the image in a microscope with point-like excitation and a large detector is far more complicated than the image formation in a confocal system (with a point-like detector). The reason is that the image formation is partially coherent. Both extremes can be mathematically described as follows:

$$I = |h_1|^2 \otimes |\tau|^2 \quad \text{incoherent image formation} \quad (1.11)$$

$$I = |h_1 \otimes \tau|^2 \quad \text{coherent image formation} \quad (1.12)$$

The difference between both cases is that for an incoherent image formation the intensities and for the coherent image formation the amplitudes have to be added. This difference can be illustrated with the following example. Consider the image formation of two points separated by the distance of the Rayleigh limit.¹¹

For the incoherent image formation, the two points are easily resolved (minimum). In the case of the coherent image formation, both points can no longer be separated (see Fig. 1.6).

¹¹ The Rayleigh criterion says that two points can be optically resolved if one point sits in the first minimum of the PSF of the second point.

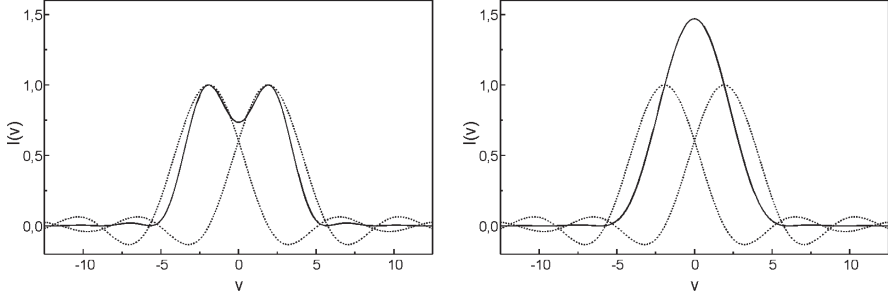


Fig. 1.6 Intensity distribution of two points that fulfill the Rayleigh criterion: *left*, incoherent image formation after (1.11); *right*, coherent image formation after (1.12)

The imaging quality of the detection described by function h_2 is not important here.

1.6.2 Confocal Microscope

Due to the point-like excitation and detection, the image formation in a confocal microscope must be described as coherent. This can be illustrated using the following equation after [6]:

$$I = |(h_1 h_2) \otimes \tau|^2 \quad (1.13)$$

The product $h_{\text{eff}} = h_1 h_2$ is called the effective PSF of the optical system. If one inserts the delta function $\delta(x)$ for τ , one gets the intensity point spread function. This function is plotted in Fig. 1.7 for a conventional and a confocal microscope. The FWHM differs roughly by a factor of $\sqrt{2}$.

1.6.3 Confocal Raman Microscope

The image formation of a confocal Raman microscope is strongly different from the case in Sect. 1.6.2. This is due to the nature of Raman scattering.

The Raman scattering is proportional to the excitation intensity $|h_1|^2$ and the Raman generation $f(x, y, z)$. The resulting equation for the intensity distribution of the resulting image in a confocal Raman microscope is therefore [7]

$$I = |h_{\text{eff}}|^2 \otimes f \quad (1.14)$$

with

$$\begin{aligned} h_{\text{eff}} &= h_1(u, v) h_2\left(\frac{u}{\beta}, \frac{v}{\beta}\right) \\ \beta &= \frac{\lambda_2}{\lambda_1} \end{aligned}$$

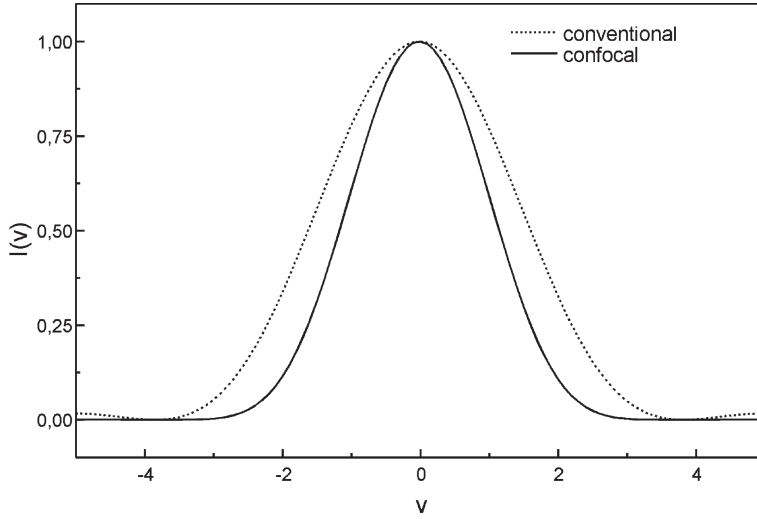


Fig. 1.7 Comparison of the intensity PSFs: $I_{\text{conventional}} = \left(\frac{2J_1(v)}{v}\right)^2$, $I_{\text{confocal}} = \left(\frac{2J_1(v)}{v}\right)^4$

The optical coordinates u and v refer to the wavelength λ_1 of the excitation light. This theory is not completely correct, because the wavelength of the Raman light has a certain frequency distribution and not only a single wavelength λ_2 . In principle, one must integrate over all Raman wavelengths. If the Raman wavelength is mostly distributed around a certain wavelength λ_x the error will be small if one replaces λ_2 with λ_x . A complete Raman spectrum is very complicated and for an exact solution the complete spectrum has to be taken into account.

1.7 Image Formation for Light Scattering

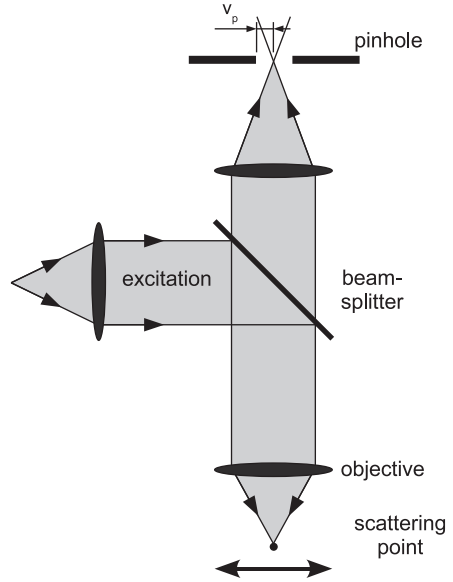
In the following two sections, the resolution of a confocal microscope as a function of pinhole size will be discussed. Since the achievable resolution strongly depends on the sample properties, these statements cannot be taken as valid in general but are true only under ideal conditions. For all calculations, the point spread function $h(u, v)$ (1.10) was used.

1.7.1 Scattering Point

In the following, we consider the scenario of Fig. 1.8 in which a scattering point is scanned laterally across the excitation focus.

Up to now, all calculations have been performed for an infinitesimally small point detector. Now we replace this point detector with a real 2D detector of radius v_p .

Fig. 1.8 Confocal setup for a scattering point



This is the reason why the PSF h_2 in (1.15) has to be convolved with the detector function D to obtain the effective PSF for the detection.

Since we consider only a single scattering point in the object space, the convolution with the object itself is not necessary. After [8] we obtain the intensity distribution through

$$I = |h_1|^2(|h_2|^2 \otimes D) \quad (1.15)$$

The FWHM of $I(u = 0, v)$ is plotted in Fig. 1.9 as a function of the detector radius v_p . As can be seen, the detector radius should be below $v_p = 0.5$ for highest resolution. If the detector radius is larger than approximately $v_p = 4$, the resolution

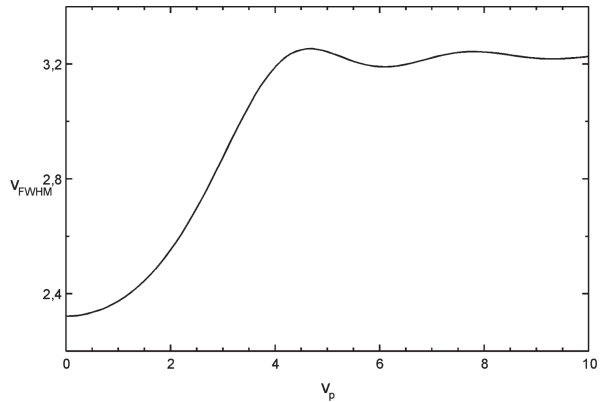


Fig. 1.9 Lateral resolution of a scattering point as a function of detector size v_p

will be the same as for conventional microscopy. Even in this case, stray light suppression remains as an advantage over conventional microscopy.

1.7.2 Reflection at a Mirror

The quality of the image can be easily checked by acquiring the signal while a mirror is scanned axially through the focus (Fig. 1.10).

Since the entire mirror plane reflects the light, the following integral [8] must be calculated:

$$I_{\text{plane}}(u) = \int_0^{v_p} |h(2u, v)|^2 v dv \quad (1.16)$$

From Fig. 1.11 one can see that there is no loss in depth resolution up to a detector radius of $v_p = 2.5$. If the detector radius gets larger than $v_p = 3.5$ the depth resolution decreases linearly with increasing detector radius.

The depth resolution of a reflecting point shows a different behavior. For small detector radii, the resolution is worse than for a reflecting layer, but for larger radii the width becomes nearly constant. At $v_p = 10$, the depth resolution is no better than for a conventional microscope with point-like excitation, but if a homogeneous layer is investigated, no axial resolution is possible with a conventional microscope.

Since no lens aberrations are taken into account, (1.16) is symmetric to $u = 0$. In reality, the distribution usually looks different. There will be drastic deviations

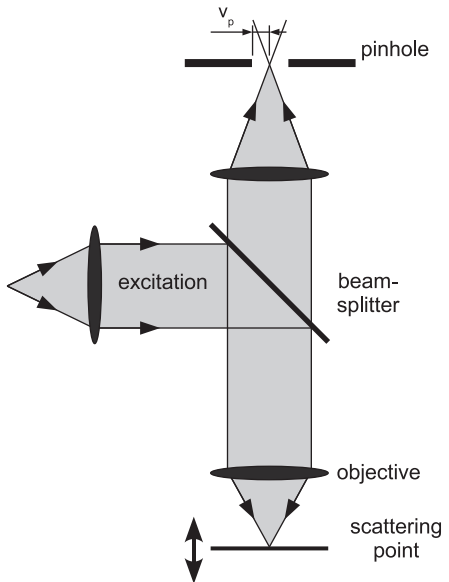
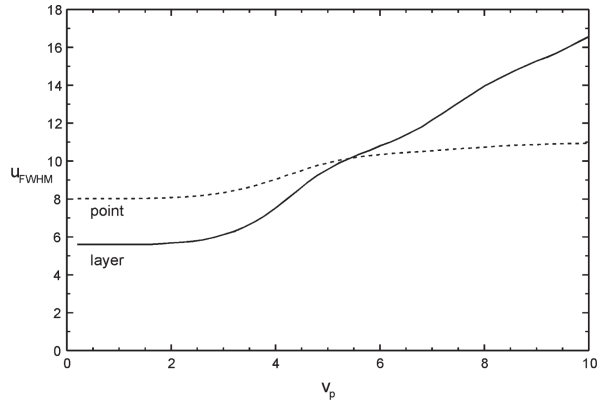


Fig. 1.10 Confocal setup for reflection at a mirror surface

Fig. 1.11 Comparison of the depth resolution for a point and a reflecting layer as a function of detector size v_p



if the setup is not optimized for the objective or the cover glass correction is not considered. An incorrect pinhole position is also immediately visible.

1.8 Image Formation for Raman Scattering

As discussed in Sect. 1.6.3, the image formation for Raman emissions is very different from the case of a scattering object. As an example, the resolution for a Raman emitting point and a Raman emitting layer will be calculated analogue to the last section.

1.8.1 Raman Emitting Point

Equation (1.14) is the basis for the curves shown in Fig. 1.12. v_p is the detector radius.

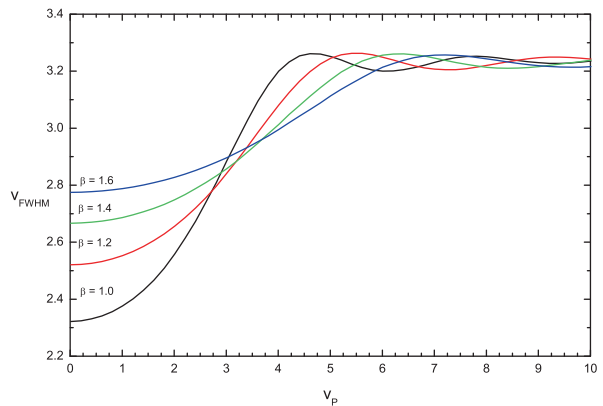


Fig. 1.12 Lateral resolution for a Raman emitting point as a function of detector size v_p for different β

The Raman emission wavelength is usually shifted by a certain factor relative to the excitation wavelength. This is taken into account by the parameter β , which is the ratio between the Raman and excitation wavelengths. For $\beta = 1$ the resolution is the same as for a scattering point. With increasing shift of the Raman wavelength, the resolution decreases. If a small loss in resolution is accepted, one sees that the pinhole size should not be adjusted to the excitation, but to the Raman wavelength. If the wavelength shift is large, one should use a larger pinhole in order to avoid an unnecessary loss in signal.

For large pinhole sizes, all curves converge. Here again the case of a conventional microscope with point-like excitation is approached. In this case, the resolution is determined only by the excitation wavelength.

For 532 nm excitation, β is between 1 and 1.25, while for 785 nm excitation β can be as high as 1.4 (at 3600 rel. cm^{-1}).

1.8.2 Raman Emission of a Layer

The axial resolution at a Raman emitting layer differs strongly from the resolution at a reflecting surface. The reason is not mainly due to the wavelength shift but rather due to the incoherent image formation.

To calculate the axial point spread function $I_{\text{CF}}(u)$ of a Raman emitting layer in a confocal microscope, one must integrate over the intensity point spread function $I(u, v, \beta)$ (after [9]):

$$I_{\text{CF}}(u) = \int_0^\infty I(u, v, \beta) v dv$$

The best depth resolution achievable at a reflecting surface was $u = 5.6$, whereas the best depth resolution for a Raman emitting layer without a wavelength shift is only

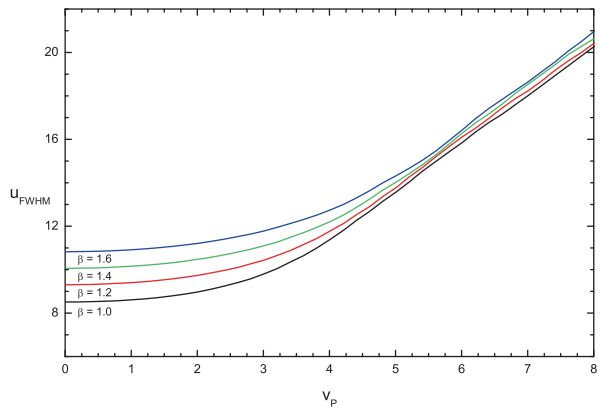


Fig. 1.13 Depth resolution at a Raman emitting layer for different β as a function of detector size v_p

$u = 8.5$ (Figs. 1.11 and 1.13). This becomes even worse with increasing wavelength shift β . Again, the detector size can be up to $v_P = 2.5$ without a loss in resolution.

1.9 Pinhole Size

Confocal microscopes typically have two output ports where one output port is equipped with an adjustable fiber coupler for multi-mode fibers or an adjustable pinhole. The core of the multi-mode fiber acts as a pinhole for confocal microscopy in the first case. The system needs to allow for lateral adjustment of the fiber so that maximum collection efficiency can be achieved.

The fiber additionally needs to be protected against mechanical strain and shielded from room light. With the fiber it is simple to direct the light to any detector, e.g., a PMT or a spectrometer.

The lateral position of the pinhole must be adjusted with micrometer precision (typical pinhole size 10–100 μm) while the focus position is not very critical.

If ΔG is the object size and M the magnification of the objective, then the lateral image size is given by $\Delta B = \Delta G \cdot M$. But what about the axial magnification? From the image equation for thin lenses one gets the relation

$$\begin{aligned} |\Delta b| &\approx |\Delta g| M^2 \\ \Delta b &\ll b && : \text{image distance} \\ \Delta g &\ll g && : \text{object distance} \end{aligned} \quad (1.17)$$

Without the diffraction limit, an object of an axial extension of 200 nm would have a length of 2 mm in the image space at a magnification of $M = 100$. Since the magnification M is quadratic in (1.17), the depth of focus is very high and the axial position of the pinhole is not critical.

The choice of the pinhole size is very important in Raman experiments. On one hand the signal should be as high as possible, while on the other hand the image should be confocal.

The size of the pinhole, in optical coordinates, should not exceed $v_{P_{\max}} = 2.5$ to avoid a loss in z -resolution. To obtain the highest lateral resolution, the pinhole size should be below $v_{P_{\max}} = 0.5$.

In practice, the pinhole size can be up to $v_{P_{\max}} = 4$ without significantly changing depth resolution and up to $v_{P_{\max}} = 2$ without significantly changing lateral resolution. As shown in Sect. 1.7.1, for $v_{P_{\max}} > 4$, only the resolution of a conventional microscope remains.

For the experiment, the relation

$$\frac{M}{NA} \geq \frac{\pi d_0}{v_{P_{\max}} \lambda}$$

must be fulfilled, where M is the magnification, d_0 the diameter of the pinhole, and NA the numerical aperture of the objective. The left side of this equation is defined

by the objective and the beam path. In Table 1.1, the parameter $\frac{M}{NA}$ is calculated for several typical objectives.

Table 1.1 M/NA for different objectives

Objective	10/0.25	20/0.4	40/0.6	60/0.8	100/0.9	100/1.25	100/1.4
M/NA	53	50	67	75	111	80	71

The right side of (1.9) is defined by the wavelength and the pinhole size itself (Table 1.2).

Table 1.2 $\frac{\pi d_0}{2.5\lambda}$ for typical wavelengths and pinhole sizes

Wavelength (nm)	440	488	532	633	785
$d_0 = 10 \mu\text{m}$	29	26	24	20	16
$d_0 = 25 \mu\text{m}$	71	64	59	50	40
$d_0 = 50 \mu\text{m}$	142	129	118	99	80
$d_0 = 100 \mu\text{m}$	286	258	236	199	160
$d_0 = 200 \mu\text{m}$	571	515	472	397	320

With the help of these tables, the correct pinhole size can be determined for any experiment. If an objective with a magnification of $100\times$ and a numerical aperture of 0.9 is used at a wavelength of 633 nm, the optimum pinhole size would be $50 \mu\text{m}$ for maximum depth resolution and $10 \mu\text{m}$ for maximum lateral resolution.

In real experiments, one must usually find a compromise between resolution and collection efficiency. When a very small pinhole is used, the collection efficiency is strongly reduced. This is plotted in Fig. 1.14.

This graph shows the intensity on the detector as a function of pinhole size, normalized to the total intensity in the image plane ($u = 0$ in (1.16)). One can see that the collection efficiency is about 75% for maximum depth resolution ($v_p = 2.5$), but only 6% for maximum lateral resolution $v_p = 0.5$.

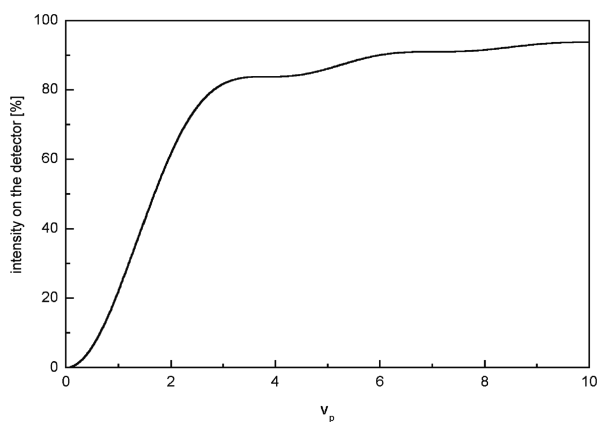


Fig. 1.14 Collection efficiency as a function of pinhole size normalized to the total power in the image plane

For a scattering point (Sect. 1.7.1, $\beta = 1$), the gain in resolution between using a pinhole size of $v_p = 2.5$ and 0.5 is only about 16%, while for a Raman emitting sample with $\beta = 1.2$ (Sect. 1.8.2) the gain in resolution is only about 8%, but for both cases the detected intensity is reduced by a factor of 12.5.

References

1. J.B. Pawley, *Handbook of Biological Confocal Microscopy*, 2nd edn. (Plenum Press, New York, 1995)
2. E. Wolf, Proc. R. Soc. London A **253**, 358 (1959)
3. E. Wolf, Proc. Phys. Soc. **74**, 269 (1959)
4. B. Richards, E. Wolf, Proc. R. Soc. London A **253**, 358 (1959)
5. R. Juškaitis, T. Wilson, J. Microsc. **189**, 8 (January 1998)
6. T. Wilson, *Confocal Microscopy*, Chap. IV.2. The imaging of simple objects (Academic, London, 1990) pp. 25–30
7. T. Wilson, *Confocal Microscopy*, Chap. IV.2. The imaging of simple objects (Academic, London, 1990) pp. 41–45
8. T. Wilson, A.R. Carlini, Opt. Lett. **12**, 227 (April 1987)
9. C.J.R. Sheppard, M. Gu, Optik **86**(3), 104 (1990)

Confocal Raman Microscopy

Dieing, Th.; Hollricher, O.; Toporski, J. (Eds.)

2011, XVI, 292 p., Hardcover

ISBN: 978-3-642-12521-8